J Sol-Gel Sci Technol (2010) 56:219–226
DOI 10.1007/s10971-010-2297-3

ORIGINAL PAPER

# Synthesis and characterization of $TiO_2$ doping with rare earths by sol–gel method: photocatalytic activity for phenol degradation

**D. de la Cruz Romero · G. Torres Torres · J. C. Arévalo · R. Gomez · A. Aguilar-Elguezabal**

Received: 26 December 2009 / Accepted: 17 July 2010 / Published online: 4 August 2010


**Abstract** The enhancement of $TiO_2$ photocatalyst activity will lead to more practical applications of this technology. In this work we studied the effect of rare earth doping of sol–gel synthesized $TiO_2$ for phenol degradation and we compared the performance with commercial catalyst. Photocatalysts were characterized by nitrogen adsorption to determine textural properties, ultraviolet visible light diffuse reflectance spectrometry (UV-Vis DRS), X-ray diffraction, STEM-EDS (scanning transmission electronic microscopy-energy dispersive X-ray spectroscopy) and XPS (X-ray photoelectron spectroscopy). Main phase for materials calcined at 500 °C was anatase. Residual nitrogen from $NH_4OH$ used in the sol–gel synthesis was identified by XPS analysis. $Ti^{3+}/Ti^{4+}$ ratio increased when $TiO_2$ was doped with 0.5 wt% of Ce. Anatase phase was stabilized in photocatalysts doped with La even after calcination at 800 °C, for Pr and Nd a mixture of anatase-rutile phases was obtained, whereas for Ce doping only rutile phase was found. For the photocatalytic oxidation of phenol, the best results were obtained for Ce doped $TiO_2$, which could be related to the ability of $Ce^{IV}/Ce^{III}$ oxidation/reduction cycle.

**Keywords** Synthesis · $TiO_2$ doping · Sol–gel · Rare earths · Characterization

D. de la Cruz Romero · A. Aguilar-Elguezabal (✉)
Centro de Investigación en Materiales Avanzados S.C., CIMAV., Av. Miguel de Cervantes 120, Complejo Industrial Chihuahua, 31109 Chihuahua, CH, México
e-mail: alfredo.aguilar@cimav.edu.mx

D. de la Cruz Romero · G. T. Torres · J. C. Arévalo
Laboratorio de Catálisis Heterogénea, Área de Química, Universidad Juárez Autónoma de Tabasco, DACB, Km.-1 carretera Cunduacán-Jalpa de Méndez AP. 24, 86690 Cunduacán, Tabasco, México

R. Gomez
Laboratorio de Catálisis, Depto. de Química, Universidad Autónoma Metropolitana-Iztapalapa, DCBI, Av. San Rafael Atlixco No. 186, 09340 México, DF, México

## 1 Introduction

In the development of a commercial photocatalytic process, due to its low cost and good performance, titanium dioxide P25 from Degussa has been the main reference as photocatalyst for destruction of organic pollutants [1–4]. Nevertheless, sol–gel method for synthesis of $TiO_2$ has been widely used to design photocatalysts with better performance than P25 [5–8], and one strategy to improve results has been, the incorporation of diverse metal compounds as Fe, Ni, Cr, V, rare earths, etc., during synthesis [9–15]. In many of the works the authors report that the addition of a dopant agent in the $TiO_2$ lead to the improvement of photocatalytic activity due to the increase on the amount of formation of electron-hole pairs, and thus with the increase of population of hydroxyl radicals ($OH^{\bullet}$) formed at the $TiO_2$ surface. This high concentration of hydroxyl radicals promotes the oxidation of organic molecules from surrounding due to its prominent activity in the oxidation reactions [16, 17]. According to Xiuqin et al. and Tinghong et al. [18, 19], the doping of appropriate amount of rare earth permits an improvement of photocatalytic activity taking as a reference the undoped photocatalyst. Lanthanum has been successfully used as a dopant of photocatalyst for water splitting; however explanation of how lanthanum improves activity has not been well established [20]. Lanthanum used in the doping of $TiO_2$ for photocatalytic degradation of organic compounds also

improved results, and according to Li et al. [21], the doping induced several benefits like a higher organic compound adsorption, higher thermal stability of $TiO_2$ and enhancement of electron-hole pairs separation. Cerium oxide is not considered a photocatalyst; however, recently Zhai [22] reported the use of $CeO_2$ as photocatalyst in the degradation of acidic black dye. In conventional catalysis cerium is well known as an oxygen supplier due to its notable redox properties [23]. The doping of a mesoporous $TiO_2$ with cerium increased the surface area of $TiO_2$ and stabilized the structure inhibiting the collapse of mesopores as well as the transformation of anatase to rutile; however an improvement on photocatalytic activity was not observed [24]. As in the above mentioned case of lanthanum, when cerium was incorporated to $TiO_2$ by a sol–gel process and tested in the photocatalytic degradation of an organic compound, an improvement in adsorption capacity and separation of electron-hole pairs was found, improving thus photocatalytic activity [25]. In the same work a displacement of absorption edge from UV to visible region was observed as a consequence of cerium doping, which also contributes to the significant enhancement of photocatalytic activity of $Ce^{3+}$-$TiO_2$. According to Xie and Yuan, neodymium doping of $TiO_2$ also induced the photocatalytic activity under visible radiation for phenol degradation [26]. Su et al. [27] reported that the incorporation of praseodymium in $TiO_2$ photocatalyst induced the photocatalytic activity in visible range of radiation.

The objective of this work is to synthesize by sol–gel process $TiO_2$ and $TiO_2$ doped with rare earths (La, Ce, Nd, Pr) and study its photocatalytic activity for phenol degradation explaining activity results based on the chemical and physical modifications induced by $TiO_2$ doping.

## 2 Experimental

### 2.1 Preparation of the $TiO_2$

The $TiO_2$ was obtained by sol gel using titanium *n*-butoxide (Aldrich) as precursor. A mixture of ethanol and water was stirred and maintained under reflux at 70 °C. Ammonium hydroxide ($NH_4OH$) was added to mixture until pH 7 was obtained. Titanium *n*-butoxide was added drop wise to this solution during 3 h approximately, stirring and refluxing was maintained for the period of 24 h until gel formation. Gels were dried by means of a rotative evaporator at 70 °C under vacuum and subsequently placed into a furnace at 120 °C during 12 h. Samples were calcined at 500 and 800 °C during 4 h with a heating rate of 2 °C/min. Undoped photocatalyst is identified as $TiO_2$-SG.

### 2.2 Preparation of the $TiO_2$ rare earth doped (La, Ce, Nd, Pr)

Rare earth doping was made using nitrate salts of each element. Water solutions of these salts were prepared calculating stoichiometric amount in order to obtain 0.5, 0.3 and 0.1 wt% according to the desired composition of sample. A mixture of ethanol, water and salt solution of rare earth was stirred and maintained under reflux at 70 °C. Enough ammonium hydroxide ($NH_4OH$) was added to mixture to obtain pH 7. Titanium *n*-butoxide was added drop wise to this solution during 3 h approximately, stirring and refluxing was maintained for the period of 24 h until gel formation. The gels were dried in a rotative evaporator at 70 °C under vacuum, subsequently gels were placed into a furnace at 120 °C during 12 h. Samples were calcined at 500 and 800 °C during 4 h with a heating ramp of 2 °C/min. By this process we must know that all the amount of dopant used for the synthesis remains at oxide.

### 2.3 Specific surface area and pore diameter

The determination of the specific surface area and mean pore diameter were carried out in a Quantachrome Autosorb-3B apparatus. The data were obtained from the nitrogen adsorption isotherm. Before the measurements the samples were desorbed at 350 °C during 2 h. Measurement variability of this equipment is below 10 % of the value. Equipment is calibrated monthly using commercial standard for surface area.

### 2.4 X-ray diffraction analysis

A SIEMENS-D500 X-ray diffactometer with an anode of Cu K$\alpha$ radiation and a graphite monochromator in the secundary beam. Intensity data were measured by step scanning in the $2\theta$ ranges between 20 and 60° with a $2\theta$ step of 0.02° and a measuring time of 1 s per point**.** Crystalline structures were refined by using the data file JCPDS.

### 2.5 UV-Vis spectroscopy

By using the diffuse reflectance technique, UV-Vis spectra were measured in a Varian Cary-III Spectrophotometer coupled to an integrated sphere.

### 2.6 Scanning electron microscopy-energy dispersive spectrum (SEM-EDS)

The samples were analyzed in a JSM-5800, magnification × 25000 in general 90×, 49μA. CPS 500, 15 kV, SS:12 for semiquantitative analysis SEM-EDS.

### 2.7 X-ray photoelectron spectroscopy analysis (XPS)

The samples were analyzed in a MK (VG Scientific Microlab) II spectrophotometer using Al KR radiation (1.487 keV). Binding energies were corrected from charge effects by reference to the C(1 s) peak of carbon contamination at 285 eV and measured with a precision of 0.2 eV. For XPS analysis, the powder samples were made into pellets of 8 mm diameter employing 12 kN pressure and placed into the housing of the analyzer under ultrahigh vacuum (UHV) chamber at $10^{-9}$ Torr. The experimental data were curve fitted with Gaussian to peaks after subtracting a linear background.

### 2.8 Photocatalytic activity of phenol

A water solution with a concentration of 100 ppm of phenol was prepared. 35 mL of this solution was placed into a photoreactor, described elsewhere [28], which was previously charged with 0.25 g of $TiO_2$ and $TiO_2$ rare earths doped. Samples of liquid were taken each hour and analyzed by UV-Vis at 270 nm using a Perkin Elmer Lambda 10 spectrophotometer, which is equipped with quartz cells for liquid analysis. In all photocatalytic tests $TiO_2$ Degussa P25 was used as a reference, and for this purpose P25 was placed simultaneously under equivalent conditions and under the same lamp. Additionally samples taken each hour were analyzed by gas chromatography with a Perkin Elmer Auto System XL equipped with a packed column OV-3 (1/8in diameter, 6 ft) and FID detector was used to follow the phenol concentration changes along photocatalytic test. GC and UV analyses were compared to corroborate results. The activity tests were made with UV–vis lamp of low energy, which has a radiation distribution centered in 360 nm wavelength. Radiation intensity was measured with three radiometers and the following radiation intensities were obtained: for radiometer of high energy, with wavelength of 210 nm, intensity was 80 mW/cm$^2$; for radiometer at 310 nm, 490 mW/cm$^2$; for 360 nm, the measured intensity was 1,620 mW/cm$^2$. Considering that lamp wavelength distribution approximates to normal distribution, according to the measured radiation intensities, the lamp also emits visible radiation, (650 mW/cm$^2$ at 400 nm).

## 3 Results and discussion

### 3.1 Materials characterization

Table 1, shows the results of BET (Brunauer, Emmett and Teller) surface area measurements, pore diameter and pore volume of photocatalysts treated at 500 °C. According to previous work [29] the expected structure of $TiO_2$ was as mesoporous material, in this case all materials showed pore diameter comprised between 3.5 and 10 nm for $TiO_2$ and $TiO_2$ doped photocatalysts.

**Table 1** Surface area, pore diameter and pore volume of the $TiO_2$ and $TiO_2$ rare earth doped (La, Ce, Nd, Pr) after calcining treatment at 500 °C

| Material | $S_{BET}$ (m$^2$/g) | $V_{pore}$ (cc/g) | $D_{pore}$ (Å) |
|---|---|---|---|
| $TiO_2$-SG | 40.5 | 0.153 | 35.0 |
| $TiO_2$-Ce-0.1 | 69.7 | 0.214 | 91.1 |
| $TiO_2$-Ce-0.3 | 78.8 | 0.247 | 102.1 |
| $TiO_2$-Ce-0.5 | 70.6 | 0.248 | 101.2 |
| $TiO_2$-Pr-0.1 | 36.4 | 0.106 | 34.7 |
| $TiO_2$-Pr-0.3 | 52.7 | 0.173 | 62.9 |
| $TiO_2$-Pr-0.5 | 72.9 | 0.220 | 68.1 |
| $TiO_2$-La-0.1 | 77.3 | 0.159 | 50.3 |
| $TiO_2$-La-0.3 | 86.3 | 0.177 | 47.7 |
| $TiO_2$-La-0.5 | 138.1 | 0.268 | 82.6 |
| $TiO_2$-Nd-0.1 | 52.0 | 0.132 | 58.5 |
| $TiO_2$-Nd-0.3 | 46.4 | 0.145 | 35.2 |
| $TiO_2$-Nd-05 | 50.5 | 0.127 | 58.5 |

Surface area increased at higher content of rare earth for Ce, Pr and La doping; the higher surface area was obtained for $TiO_2$ doped with $La^{3+}$ at 0.5 wt%. This surface area corresponds to more than three times the value obtained for undoped $TiO_2$ ($TiO_2$-SG). The increase of surface area could be explained by a high dispersion of rare earth and the fact that the ionic radii of the rare earths used in this case are larger than $Ti^{4+}$. These values are 1.15 Å for $La^{3+}$, 1.03 Å for $Ce^{3+}$, 1.01 Å for $Nd^{3+}$, 1.09 Å for $Pr^{3+}$ and 0.64 Å for $Ti^{4+}$ [30]. Substitution of the rare ions on $TiO^{4+}$ lattice of anatase structure, formed Ti-O-M bonds, where M represents the rare earth ion (M = La, Ce, Nd, Pr), modifying thus the arrangement of the structure and as a result the BET surface area.

In Table 2, the results of the surface area, pore volume and pore size diameter for samples treated at 800 °C are shown. In this case, only the samples with 0.5 wt% of rare earth were treated at 800 °C. It can be observed that for all

**Table 2** BET surface areas, pore diameter and pore volume of the $TiO_2$ and rare earths doped $TiO_2$ (La, Ce, Nd, Pr) treated at 800 °C

| Material | $S_{BET}$ (m$^2$/g) | $V_{pore}$ (cc/g) | $D_{pore}$ (Å) |
|---|---|---|---|
| $TiO_2$-Ce-0.5 | 4.4 | 0.058 | 183.7 |
| $TiO_2$-Pr-0.5 | 21.3 | 0.088 | 159.3 |
| $TiO_2$-La-0.5 | 39.2 | 0.193 | 132.3 |
| $TiO_2$-Nd-0.5 | 8.3 | 0.042 | 153.3 |

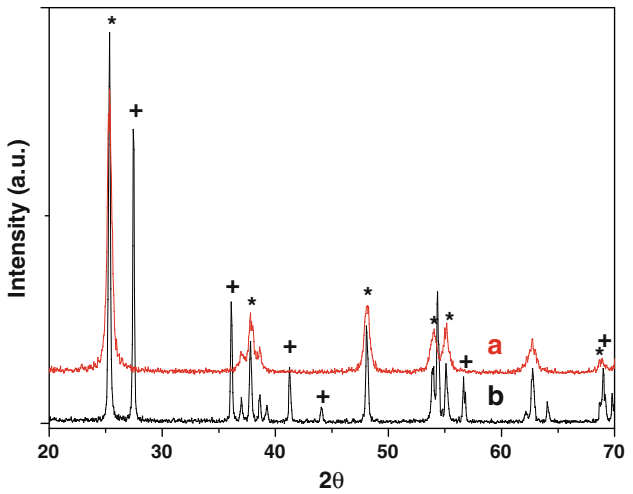


**Fig. 1** X-Ray diffraction patterns of: **a** $TiO_2$-500 °C, **b** $TiO_2$-800 °C. (*) Anatase, (+) Rutile

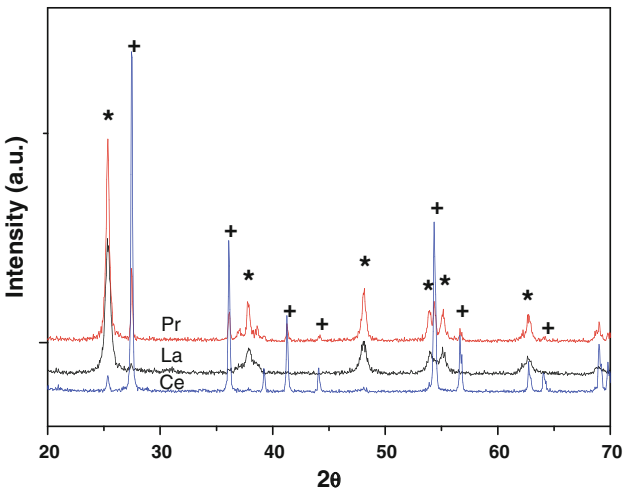


**Fig. 2** X-Ray diffraction patterns of: **a** $TiO_2$-Pr (0.5 wt%), **b** $TiO_2$-La (0.5 wt%) **c** $TiO_2$-Ce (0.5 wt%) calcined at 800 °C. (*) Anatase, (+) Rutile

the samples the surface area decrease in comparison with the values obtained by the samples treated at 500 °C. The phenomena can be explained by growth of crystal size and the beginning of sintering process. These phenomena are well known for thermal transformation of anatase to rutile phase, which normally occur around 700–800 °C for undoped $TiO_2$ [31, 32]. During the thermal treatment, the coalescence of pores was obtained which is indicated by the increase of the diameter of pore, as well as the drastic reduction of pore volume (with the exception of La doped sample).

In order to study the structural characteristics of photocatalysts, X-ray diffraction analysis was made to samples. For all the samples calcined at 500 °C only anatase phase was observed from XRD diffractograms. The results of X-ray diffraction of undoped $TiO_2$ photocatalyst (Fig. 1) reveal that under calcining treatment at 500 °C only anatase phase was formed. After the treatment at 800 °C a mixture of anatase-rutile phases appear. Rare earth doping of $TiO_2$, seems to stabilize anatase structure on $TiO_2$ allowing a slow phase transition during thermal treatments, even at 800 °C, where typically the presence of anatase is not found, but rutile [33].

The XRD spectra of $TiO_2$ rare earth doped with La, Pr and Ce and treated at 800 °C are shown in the Fig. 2. As can be seen, La addition stabilizes completely the anatase phase. For $TiO_2$ Pr doped, lower anatase phase stability was induced. Otherwise, Ce ion seems to promote the transition anatase-rutile since almost all anatase peaks disappear after treatment at 800 °C, contrary to the results observed by Xiao et al. [24] and Francisco et al. [32]. Main difference with those works is the high dispersion of cerium obtained in our work, since after calcining treatment at 800 °C cerianite phase was not present, whereas the development of cerianite seems to be necessary to stabilize anatase phase for $TiO_2$-Ce.

$TiO_2$-La shown only the anatase phase, and $TiO_2$-Nd shown a mixture of anatase-rutile phases, being predominant the rutile phase. Lin et al. [34] studied previously the anatase phase transition to rutile; in their results the XRD spectra showed that the presence of the $La_2O_3$, $Y_2O_3$ and $CeO_2$ at 0.5 wt% stabilized the anatase phase at 650 °C for La, and at 700 °C for Y and Ce. They explained this phenomenon by the fact that in the interface, the titanium atoms replace the elements of rare earth in the rare earth oxide surface to form tetragonal sites of the titanium atoms. A similar explanation was reported by another group of researchers [35]. They explained for the case of the $TiO_2/SiO_2$ (ratio 30/70) that the stabilization of the anatase phase occurs by the biphasic covering of the $SiO_2$ in the bond Ti-O-Si. The silicon atoms are replaced within the tetrahedral $SiO_2$ forming tetrahedral sites of Ti. Thus, the restraining of anatase-rutile phase transformation is attributed to the interaction between octahedral-tetrahedral sites. However, considering that in this work the synthesis of materials was made by sol–gel, the formation of isolated rare earth crystals to form interface surfaces with $TiO_2$ is not probable, so the mechanisms of anatase stabilization must be related to the lack of mobility induced by the integration of some atoms of rare earth on the crystalline structure.

Table 3 shows band gap obtained from UV-Vis spectra taken by DRS to the samples under study. For calcined $TiO_2$ at 500 °C, the band gap is 2.92 and 2.72 eV for $TiO_2$ calcined at 800 °C. For doped samples, the highest band gap was presented by cerium doped photocatalyst (3.07 eV), whereas the lower value was for praseodymium doping before calcination (2.97 eV). For 0.1 wt%

**Table 3** Band gap calculated by reflectance diffuse UV-Vis

| Photocatalyst | Band gap (eV) |
|---|---|
| $TiO_2$-Sol–gel | 2.96 |
| $TiO_2$-Sol–gel[a] | 2.72 |
| $TiO_2$-Ce 0.5% | 3.07 |
| $TiO_2$-Ce 0.3% | 3.07 |
| $TiO_2$-Ce 0.1% | 3.02 |
| $TiO_2$-La 0.5% | 3.12 |
| $TiO_2$-La 0.3% | 3.00 |
| $TiO_2$-La 0.1% | 3.02 |
| $TiO_2$-Nd 0.5% | 2.99 |
| $TiO_2$-Nd 0.3% | 3.02 |
| $TiO_2$-Nd 0.1% | 2.98 |
| $TiO_2$-Pr 0.5% | 3.00 |
| $TiO_2$-Pr 0.3% | 3.00 |
| $TiO_2$-Pr 0.1% | 2.97 |

[a] Calcined at 800 °C

neodymium doping, band gap changed from 3.02 to 2.98 eV after calcining treatment and for praseodymium, instead of decreasing an increase was obtained from 2.97 to 3.0 eV. Thus for all calcined samples, required light radiation have to be preferably UV than visible radiation for photocatalytic tests.

In the Fig. 3 the SEM-EDS analysis of $TiO_2$ doped with 0.5 wt% Ce is shown. A high dispersion of Ce was found when elements distribution was determined by EDS mapping (3b), this high dispersion could be correlated with the increase of surface area when rare earths are incorporated on $TiO_2$. Ce was measured by EDS (3a) and it was established that sol–gel technique permit incorporate all the theoretical rare earth desired with a good dispersion on the material, which explains the absence of cerianite even after calcining treatment. As can be seen from the SEM image showed in the Fig. 3d, a polymorphous material was obtained by this sol–gel synthesis.

XPS spectra of $TiO_2$ and $TiO_2$ doped with 0.5 wt% of Ce are shown in the Figs. 4 and 5. As can be seen, the intensity of the peak corresponding to N is more pronounced in the $TiO_2$ than $TiO_2$ with 0.5 wt% of Ce. The N found in these samples was attributed at the fact that in the sol–gel synthesis $NH_4OH$ was used as hydrolysis catalysis. The Table 4 shows the results of the XPS analysis made to $TiO_2$ and $TiO_2$ 0.5 wt% Ce. The $N/(Ti^{3+} + Ti^{4+})$ ratio is significantly higher for undoped sample. This can be explained by the fact that when Ce is present in the synthesis, there is a competition with nitrogen to diffuse on crystalline structure. When the $TiO_2$ is free of cerium the peak corresponding to the $Ti^{3+}$ is practically null, being $Ti^{4+}$ the main signal (see Table 4). Contrary at the $TiO_2$-SG when Ce is present, the area of $Ti^{3+}$ becomes important and area is almost the same of $Ti^{4+}$ ($Ti^{3+}/(Ti^{3+} + Ti^{4+}) = 0.52$). The most important result obtained with XPS analysis was the verification of the presence of the N into the materials, and as is well known, the presence of N on $TiO_2$ structure induce a lower band gap energy, which could explain that undoped $TiO_2$ presented a band gap energy value lower than 3 eV, when typically this value is higher than 3 eV. The contribution of this shift, for the other samples highly depend on the rare earth, since $TiO_2$ was co-doped with N + M (where M denote the rare earth) and both elements have an effect on the titania structure that can affect band gap value.

### 3.2 Photocatalytic activity of phenol

Figure 6 shows phenol conversion under photocatalytic degradation for samples prepared with a dopant content of 0.1 wt% and the activity of $TiO_2$-P25 was also included as a reference in each activity test. As can be seen only cerium doped catalyst presented higher conversion than $TiO_2$-P25 after 10 h of reaction and the slope at the end of activity measurement indicates that the advantage over P25 will be maintained for prolonged reaction times. The comparison of photocatalytic activity among sol–gel prepared materials permits to determine that excepting the use of praseodymium in all cases the activity was higher for doped materials than undoped after 10 h of reaction being the reaction activity as follows:

$$TiO_2 - Ce > TiO_2 - P25 > TiO_2 - La > TiO_2 - Nd > TiO_2 - Pr = TiO_2 sol - gel$$

As it can be observed in the Table 3, band gap values increase in the same order that photocatalytic activity. The highest activity after 10 h of the reaction was for $TiO_2$-Ce, which presented the highest band gap value (3.02). In spite of the same value of band gap presented by $TiO_2$-P25 and Ti-La these materials were less active for phenol degradation than $TiO_2$-Ce. For the other materials activity was lower. The match between photocatalytic activity and band gap is due to the higher range of activation in the UV/Vis spectrum for materials with higher band-gap, which agrees with the intensity distribution of radiation of the lam used for these experiments. For future experiments using radiation lam with higher visible/UV ratio it could be expected that the materials with lower band gap values will shown the best performance to mineralize organic compounds.

Another mechanism for the improvement of photocatalytic activity is the increase of vacancies on the oxide structure as in the case of cerium oxide dopant [36]. In such case, the pair of $Ce^{3+}/Ce^{4+}$ oxide-reduction is well established and has carried out an additional role in the properties of the photocatalyst [37]. Another explanation of the major performance of Ce dopant was established due at the

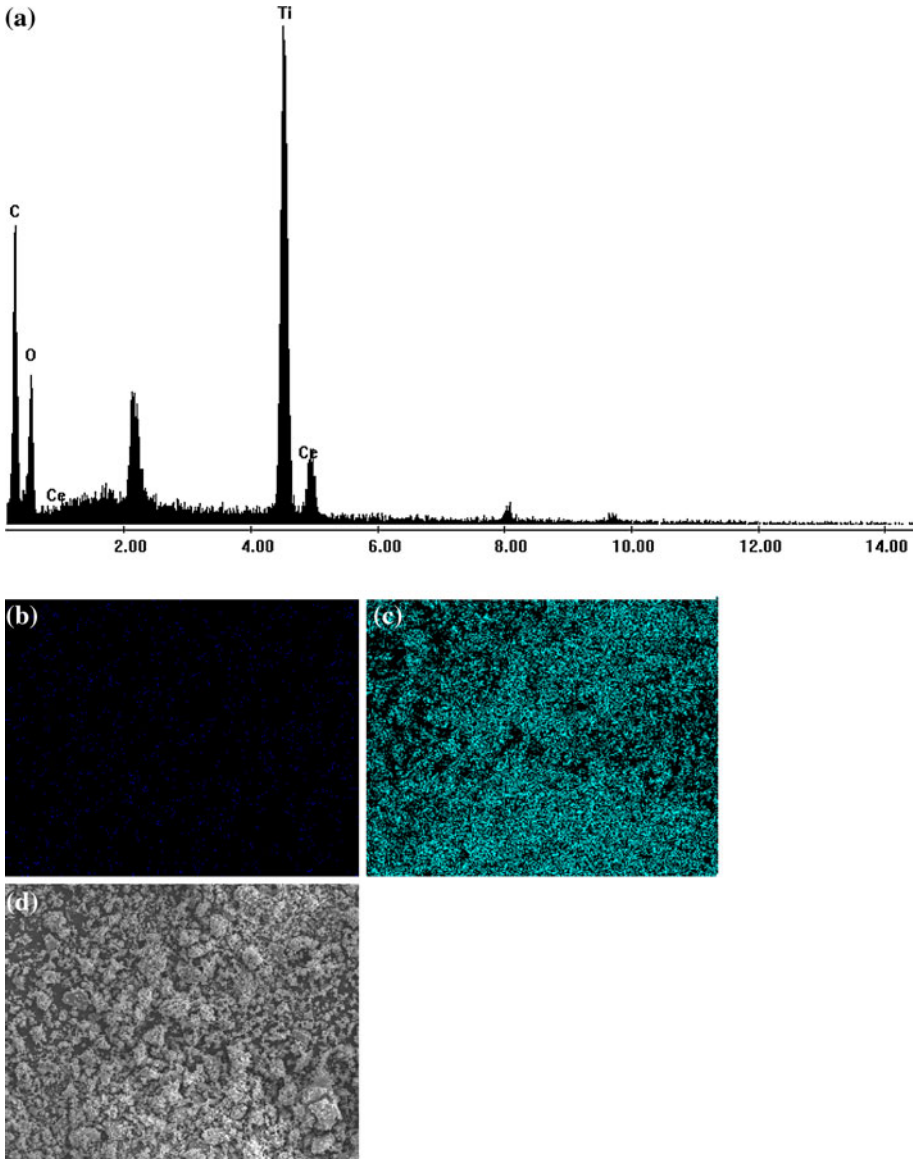


**Fig. 3** SEM-EDS analysis. **a** EDS spectrum, **b** mapping of Ce distribution, **c** mapping of Ti distribution, **d** SEM of $TiO_2$ with 0.5 wt% of Ce

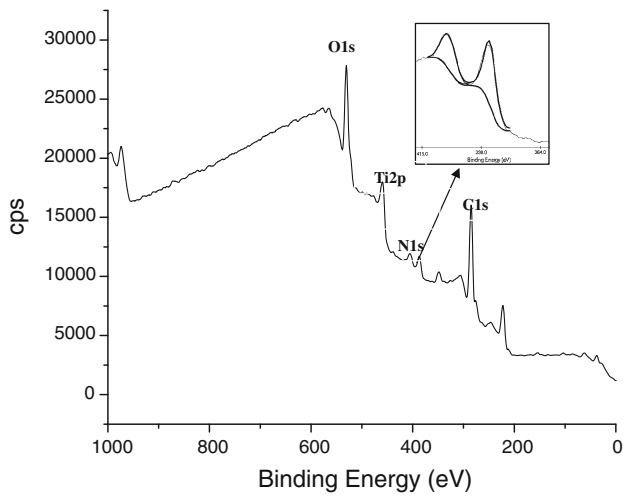


**Fig. 4** XPS survey spectrum of undoped $TiO_2$

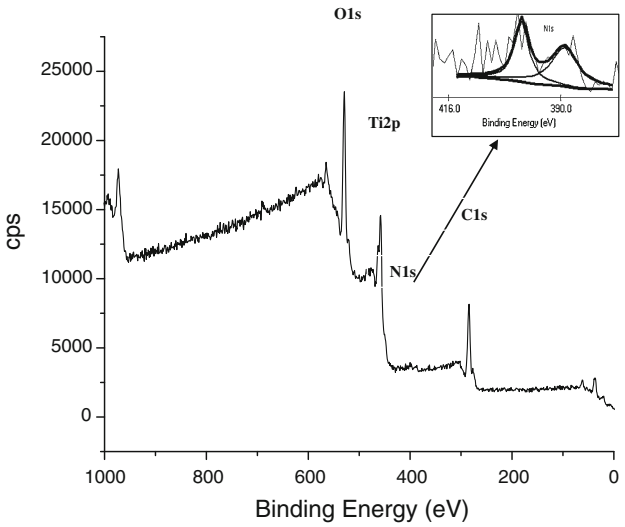


**Fig. 5** XPS survey spectrum of 0.5 wt% $Ce/TiO_2$

**Table 4** XPS binding energy and peak area values for the $TiO_2$ samples calcined at 500 °C

| Material | N BE (eV) | Peak area (N) | $Ti^{3+}$ BE (eV) | Peak area ($Ti^{3+}$) | $Ti^{4+}$ BE (eV) | Peak area ($Ti^{4+}$) | $Ti^{3+}$ / $Ti^{3+}+Ti^{4+}$ | N / $Ti^{3+}+Ti^{4+}$ |
|---|---|---|---|---|---|---|---|---|
| $TiO_2$-SG | 404.2 | 5,925.5 | 456.38 | 0.6 | 457.974 | 53,575.2 | 0 | 0.110 |
| $TiO_2$-Ce0.5 | 399.0 | 3,110.4 | 456.26 | 33,289.3 | 458.445 | 30,472.0 | 0.52 | 0.049 |

*BE* binding energy

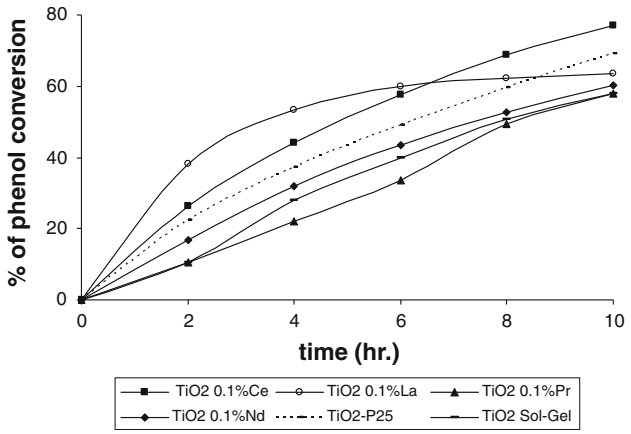


**Fig. 6** Photocatalytic oxidation of phenol using $TiO_2$ doped rare earth (La, Ce, Nd, Pr) at 0.1 wt%. Phenol concentration = 100 ppm, 0.35 g $TiO_2$-M and 35 mL of solution

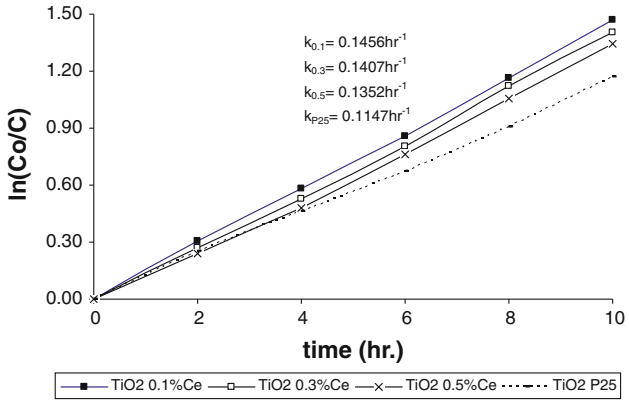


**Fig. 7** Linear transform In Co/C = $f$(t) of the kinetics of phenol disappearance during reaction using $TiO_2$ Degussa P25 powder and $TiO_2$ doped Ce with 0.1, 0.3 and 0.5 wt% respectively. Phenol concentration = 100 ppm, 0.35 g of photocatalyst and 35 mL of solution

**Table 5** Photocatalytic activity of undoped and doped $TiO_2$ for phenol mineralization

| Material | % Maximum degradation after exposition time of 10 h | | | |
|---|---|---|---|---|
| | Undoped | 0.1 wt% | 0.3 wt% | 0.5 wt% |
| $TiO_2$-P25 | 60 | | | |
| $TiO_2$-SG | 51 | | | |
| $TiO_2$-Ce | – | 69 | 67 | 65 |
| $TiO_2$-La | – | 62 | 50 | 59 |
| $TiO_2$-Pr | – | 49 | 61 | 42 |
| $TiO_2$-Nd | – | 53 | 51 | 68 |

fact that $Ce^{4+}$ showed strong absorption in the UV-Vis range [38].

It can be observed in the Table 5 that for each dopant there is a specific concentration at which photocatalytic activity is maximum, thus for lanthanum and cerium maximum activity was observed for photocatalyst doped with 0.1 wt%. For neodymium the best results were obtained at content of 0.5 wt%, whereas for praseodymium the higher activity was obtained with a content of 0.3 wt%. We can see that for all cases Ce doped photocatalysts presented high activity. Li et al. [25] proposed that the formation of two sub-energy levels (defect level and Ce 4f level) in $Ce^{3+}$-$TiO_2$ might be a key reason to eliminate the recombination of electron-hole pairs and to enhance the photocatalytic activity. Ce performance also has been explained by its capacity to supply oxygen to milieu by oxidation/reduction ($Ce^{4+}/Ce^{3+}$) cycle, which increases the population of oxidant species at photocatalyst surface [16]. It can be established that because the ionic radius of Ce(IV) (0.92 Å) is larger than that of Ti (IV) (0.64 Å) but smaller than oxygen (1.32 Å), the cerium ions can be introduced by Ti substitution into the matrix, producing some deformation of the lattice structure and deformation energy [39].

Figure 7 shows the photocatalytic behavior of the $TiO_2$ Degussa P25 and $TiO_2$-Ce doped powder photocatalysts with 0.1, 0.3 and 0.5 wt% respectively, in the degradation of phenol. For these results obtained we assumed that photocatalytic oxidation of organic pollutants in the aqueous solution follows Langmuir-Hinshewood model [40, 41]. Constant kinetics $k$ values obtained by plotting $Ln(C_0/C)$ vs time showed that the optimal quantity of cerium was 0.1 wt% because the most high $k$ value was obtained when this photocatalyst was used in the phenol oxidation. In all cases the $k$ values for Ce doped photocatalysts was higher than commercial P-25. Catalytic results presented in this figure suggest that the overall reaction occurs following an apparent pseudo-first kinetic order with respect to phenol for all cases [40].

## 4 Conclusions

$TiO_2$ was synthesized by sol–gel and doped with rare earths. Doped materials presented better textural properties like higher surface area, pore volume and pore diameter than undoped $TiO_2$. Nitrogen from $NH_4OH$ used in the sol–gel synthesis was detected by XPS and could contribute to the displacement of $TiO_2$ band gap to lower values. Band gap for rare earth doped materials did not changed significantly, and the observed trend was that rare earth doping increased band gap due to a lower N quantity remaining in the oxide. The typical transformation of anatase phase to rutile by thermal treatment was partially inhibited for neodymium and praseodymium and almost totally inhibited for lanthanum at a content level of 0.5 wt%, nevertheless a promote effect of this phase change was observed for cerium doping, attributed at the nucleation phenomena because a polymorphous material was obtained with this dopant which emphasize the transformation of anatase to rutile. Cerium doping shown the best results for photocatalytic activities and for the three concentrations used, the activities were higher than the observed for DP-25. For cerium and lanthanum the doping of $TiO_2$ at 0.1 wt% is enough to improve results, whereas for praseodymium and neodymium the optimum content is 0.3 and 0.5 wt% respectively.

**Acknowledgments** We thank gratefully the Mexican PROMEP program for the scholarship for the MSc Durvel de la Cruz Romero. Too we thank so much for their technical support in the synthesis and analysis at Miss. Maria Matea Segovia Montejo and Miss. Graciela Díaz Oliva.

## References

1. Reyes DC, Fernández J, Freer J, Mondaca MA, Zaror C, Malato S, Mansilla HD (2006) J Photochem Photobiol A:Chem 184:141
2. Guillard C, Lachheb H, Houas A, Ksibi M, Elaloui E, Herrmann JM (2003) J Photochem Photobiol A:Chem 158:27
3. Ksibi M, Zemzemi A, Boukchina R (2003) J Photochem Photobiol A:Chem 159:61
4. Zan L, Fa W, Peng T, Gong ZK (2007) J Photochem Photobiol B:Biol 86:165
5. Hidalgo MC, Aguilar M, Maicu M, Navío JA, Colón G (2007) Catal Today 129:50
6. Jing L, Li S, Song S, Xue L, Fu H (2008) Sol Energy Mater Sol Cells 92:1030
7. Keshmiri M, Mohseni M, Troczynski T (2004) Appl Catal B:Environ 53:209
8. Gómez R, López T, Ortiz-Islas E, Navarrete J, Sánchez E, Tzompanztzi F, Bokhimi X (2003) J Mol Catal A: Chem. 193:217
9. Zhou W, Zheng Y-H, Wu GH (2006) Appl Surf Sci 253:1387
10. Xu AW, Gao Y, Liu HQ (2002) J Catal 207:151
11. Liang CH, Li FB, Liu CS, Lü JL, Wang XG (2008) Dyes Pigm 76:477
12. Araña J, Doña-Rodríguez JM, González-Díaz O, Tello Rendón E, Herrera Melián JA, Colón G, Navío JA, Pérez Peña J (2004) J Mol Catal A:Chem 215:153
13. Yu J, Zhou M, Yu H, Zhang O, Yu Y (2006) Mater Chem Phys. 95:193
14. Wang JA, Limas-Ballesteros R, López T, Moreno A, Gómez R, Novaro O (2001) J Phys Chem B 105:9692
15. Yuan Z-H, Jia J-H, Zhang L (2002) Mater Chem Phys 73:323
16. Ch Wen, Deng H, Tian J-Y, Zhang J-M (2006) Trans Nonferrous Met Soc China 16(2):728
17. Caimei F, Peng X, Yanping S (2006) J Rare Earths 24:309
18. Xiuqin O, Junping M, Qimin W, Junmei Y (2006) J Rare Earths 24:251
19. Tinghong H, Jian M, Xiaodong Z, Minding T (2006) Rare Metals 25(4):331
20. Kudo A, Niishiro R, Iwase A, Kato H (2007) Chem Phys 339:104
21. Li FB, Li XZ, Hou MF (2004) Appl Catal B:Environ 48:185
22. Zhai Y, Zhang S, Pang H (2007) Mater Lett 61:1863
23. Liu Z, Zhou R, Zheng X (2007) J Mol Catal A:Chem 267:137
24. Xiao J, Peng T, Li R, Peng Z, Yan C (2006) J Solid State Chem 179:1161
25. Li FB, Li XZ, Hou MF, Cheah KW, Choy WCH (2005) Appl Catal A:Gen 285:181
26. Xie Y, Yuan C (2004) Appl Surf Sci 221:17
27. Su W, Chen J, Wu L, Wang X, Wang FuX (2008) Appl Catal B:Environ 77:264
28. Silveyra R, e Sáenz L, Antúnez Flores W, Collins Martínez V, Aguilar Elguézabal A (2005) Catal Today 107–108:602
29. López T, Rojas F, Alexander-Katz R, Galindo F, Balankin A, Buljan A (2004) J Solid State Chem 177:1873
30. Liu Z, Guo B, Hong L, Jiang H (2005) J Phys Chem Solids 66:161
31. Ramis G, Busca G, Cristiani C, Liette L, Forzatti P, Bregani F (1992) Langmuir 8:1774
32. Francisco MSP, Mastelaro VR (2002) Chem. Mater 14:2514
33. Zhang Y, Zhang H, Xu Y, Wang Y (2004) J Solid State Chem 177:3490
34. Lin J, Yu JC (1998) Photochem. Photobiol A:Chem 116:63
35. Xu Y-H, Zeng Z-X (2008) J Mol Catal A:Chem 279:77
36. Galindo F, Gómez R, Aguilar M (2008) J Mol Catal A:Chem 281:119
37. Xie Y, Yuan C (2003) Appl Catal B:Environ 46:251
38. Yan Q-Z, Su X-T, Huang Z-Y, Ge C-C (2006) J Eur Cer Soc 26:915
39. Rodríguez R, Vargas S, Arroyo R, Montiel R, Haro E (1997) J Mat Res 12:439
40. Xu Y-H, Chen H-R, Zeng Z-X, Bo L (2006) Appl Surf Sci 252:8565
41. Hong S-S, Lee M, Lee G-D, Lim K, Ha B-J (2003) Mater Lett 57:2975